

# A Fast Distributed Data-Assimilation Algorithm for Divergence-Free Advection

Tigran T. Tchrakian<sup>\*1</sup> and Sergiy Zhuk<sup>†1</sup>

<sup>1</sup>*IBM Research – Ireland*

## Abstract

In this paper, we introduce a new, fast data assimilation algorithm for a 2D linear advection equation with divergence-free coefficients. The latter is discretised in space using the nodal discontinuous Galerkin (DG) method, which approximates the solution in non-overlapping spatial elements by Lagrange polynomials. This is used to perform data assimilation in a distributed fashion: the proposed algorithm employs a set of interconnected minimax state estimators (filters) which run in parallel on spatial elements possessing observations. The filters are interconnected by means of numerical Lax-Friedrichs fluxes. Each filter is discretised in time by a symplectic Mobius time integrator which is stable and preserves symmetry and positivity of the analog of state error covariance matrix (Riccati matrix) together with all quadratic invariants of the estimation error dynamics. The cost of the proposed algorithm scales linearly with the number of elements. This is in contrast to a “global” approach which requires the assembly of a global stiffness matrix and quickly becomes computationally intractable even for a modest number of elements. Examples are presented using both synthetic and real data. In the latter case, satellite images are assimilated into a 2D model representing the motion of clouds across the surface of the Earth.

## 1 Introduction

Data Assimilation (DA) is an important component in many modern industrial cyber-physical systems. It improves the accuracy of forecasts provided by physical models by optimally combining their states – *a priori* knowledge encoded in equations of mathematical physics – with *a posteriori* information in the form of sensor data, the so-called state estimation, and evaluates forecast reliability by taking into account uncertainty, i.e., model errors or sensor noise. Mathematically, DA relies upon optimal control methods or stochastic filtering. In the probabilistic framework, the optimal solution of the state estimation problem is given by Kushner-Stratonovich equation which describes the dynamics of the conditional probability density of the state of a Markov diffusion process given incomplete and noisy observations [7]. In contrast, deterministic state estimators assume that errors have bounded energy and belong to a given bounding set. The state estimate is then defined as a minimax center of the reachability set, a set of all states of the physical model which are reachable from the given set of initial conditions, and are compatible with observations. Dynamics of the minimax center is described by a minimax filter [10]. We refer the reader to [17, 11] for the further discussion on modern data assimilation and state estimation.

---

<sup>\*</sup>tchrakit@gmail.com

<sup>†</sup>sergiy.zhuk@ie.ibm.com

The major issue of DA approaches is the lack of scalability: indeed, computing optimal state estimates for PDEs is often infeasible even in two spatial dimensions due to the “curse of dimensionality”. To illustrate this issue consider a linear system

$$\frac{dC}{dt} = AC, \quad Y(t) = HC(t) + \eta(t), \quad C(0) = C_0,$$

where  $A$  is the physical model,  $Y$  is the sensor data corrupted by some noise  $\eta$ ,  $H$  is the mathematical representation of the sensor relating states  $C(t)$  to  $Y(t)$ , and  $C_0$  is an uncertain initial condition such that, for given symmetric positive definite operators  $Q_0$  and  $R$  it holds that:

$$(Q_0 C_0, C_0) \leq 1, \quad \int_0^T E(R\eta, \eta) dt \leq 1,$$

In this case, the optimal state estimator is given by the minimax filter:

$$\frac{d\hat{C}}{dt} = AC + PH^T R(Y - HC), \quad \hat{C}(0) = 0, \quad (1)$$

$$\frac{dP}{dt} = AP + PA^* - PH^* RHP, \quad P(0) = Q_0^{-1}, \quad (2)$$

which is, in fact, equivalent to the estimate of the Kalman filter [9]. As noted above, accurately approximating  $\hat{C}$  and the so-called gain or state error covariance operator  $P$  in real time is not feasible even if  $A$  is a linear advection-diffusion operator in two spatial dimensions: a very modest approximation of  $A$  by 100 or so basis functions in each spatial dimension will result in a  $10000 \times 10000$  stiffness matrix so that, generally speaking, the problem of finding an accurate and fast approximation of  $P$  solving the matrix differential Riccati equation (2) becomes intractable.

**Contribution** In this paper, we propose an efficient and scalable data assimilation algorithm for linear advection equations with divergence-free coefficients in two spatial dimensions. The algorithm is distributed, i.e., it uses a network of local filters which process localised observations, and then exchange portions of the information with the neighbouring filters to reconstruct the “global” state. Mathematically, the proposed algorithm relies upon the nodal Discontinuous Galerkin (DG) discretization of the advection equation: the computational domain  $\Omega$  is approximated by a set of non-overlapping elements,  $D^k$ , and the PDE is substituted by a system of ODEs which describes the evolution (in time) of a vector approximating the restriction of the solution of the PDE,  $C$  onto a grid formed by Legendre-Gauss-Lobatto quadrature points within each element  $D^k$ , (see section 3.1). Taking a large enough number of small elements with low order polynomials allows us to approximate  $C$  with high precision, and, at the same time, keep the stiffness matrices small.

For each element  $D^k$ , the minimax state estimator (filter) is applied to estimate the state of the system of ODEs by using the observations localised in  $D^k$ . The filters, located at adjacent elements, “run” independently and ‘communicate’ with one another through the boundary integrals and local Lax-Friedrichs fluxes (see section 3.2). As noted, the size of the stiffness matrices is quite small, and this allows us to use a symplectic Mobius time integrator [6] to discretize the corresponding matrix Riccati differential equation. This type of time discretization preserves symmetry and positivity of the Riccati matrix,  $P$ . In addition, all quadratic invariants of the estimation error dynamics are preserved too. The importance of this for practical applications is that the simulation results are trustworthy and represent indeed what has been predicted by the theory for the continuous case. In section 4.2 we illustrate the proposed method for one such practical case, namely data assimilation of cloud optical depth satellite images into a linear advection equation over a large spatial domain with inflow zones and incorrect advection coefficients represented by a wind field.

One of the main advantages of the proposed distributed filtering approach is its scalability, i.e. the potential for speed-up due to parallelisation of the filter over elements. Indeed, the system obtained by the DG method is solvable using a two-level time-integration scheme, where the solution or estimate at the current time-level requires only the solution at the previous time-level. The elemental solutions can thus be obtained in parallel, where for each elemental system, we need only the solution on that element at the previous time level and the local DG system matrices, which are obtained using the current advection field, boundary and initial conditions. As a result, the cost of the proposed algorithm scales linearly with the number of elements (see section 4.1.5).

In this paper the “discretize-then-optimize” strategy is used instead of discretizing an infinite dimensional filter equation directly. The main reason for this is that the optimal infinite dimensional minimax/Kalman filters are available in the literature for linear parabolic equations including advection-diffusion equations, and symmetric systems of linear hyperbolic equations in  $\mathbb{R}^n$ . Neither suits our application, namely data assimilation of cloud optical depth images into a scalar linear hyperbolic equations in a bounded domain with boundary conditions on the inflow zone. For this reason we adopt a hybrid strategy, namely discretize in space by using DG method, and do the state estimation in the continuous time by employing the minimax filter. We stress that in the linear case the state estimates provided by the Kalman and minimax filters coincide [9]. However, the interpretation of the state estimation error is different: the minimax filter assumes merely bounded model errors in contrast to the standard statistical assumptions of the Kalman-Bucy filter. Since we have to take the discretization error into account, and there is no statistical information about its distribution, the worst-case estimation error of the minimax filter appears to be more appropriate here.

Our choice of the DG method is motivated not only because of its use of elements, but also because of the way in which the elements communicate with one another through fluxes. This is a key difference between DG and the Spectral-Element Method (SEM) family of methods. Although the latter also uses an elemental discretisation, their handling of element interfaces requires the field representing the advected quantity to be smooth. This can result in problems when the methods are applied to advection-dominated flows (i.e. flows with high Peclet number), as instabilities can arise [12]. In order to overcome this issue, artificial diffusion can be added to the model, but in many cases, the amount of diffusion required may be un-physical. In contrast to SEM, the DG method relies on flux transfer between elements, which makes it more robust in advection dominated settings [14, 4, 3]. For nonlinear problems and linear advection problems where the velocity field is non-smooth, a flux limiter can be employed for DG [14]. In this paper however, we will restrict our attention to 2D advection by divergence-free velocity fields, and thus will not need to apply any post-processing to our estimates.

**State-of-the-art** The problem of finding approximations of the solution  $P$  of the matrix differential Riccati equation has been studied by many authors. The most popular statistical method is the so-called Ensemble Kalman Filter (EnKF) [5]. Using that approach the computational bottleneck in computing  $P$  is overcome by generating an ensemble of trajectories and by computing the ensemble variance to approximate the state error covariance matrix  $P$ . The latter is then used to compute a state estimate in the same way as in the Kalman filter. We stress that  $P$  is quite large even in the case of the advection-diffusion equation in two dimensions, hence, the required exhaustive sampling is hardly feasible. A different reduction strategy, a so-called square-root Kalman Filter, propagates only the leading modes of the gain, i.e. eigenvectors of  $P$  representing largest eigenvalues. This strategy can be quite successful in the case of time-invariant linear systems. However, it may fail if  $A$  is changing in time. Note that these methods focus on approximating the “global” matrix,  $P$ . In contrast, our approach is to construct very precise approximations of the “small” elemental matrices  $P$  by solving Riccati equations. The resulting approximations contain full information

about the elemental state vector which is then communicated to the neighbours by means of the boundary integral interconnection mechanism of the DG method (see section 3.2). Consequently, the “stitched” estimate approximates the solution of the PDE everywhere in  $\Omega$ . The numerical comparisons of the  $P$  computed for a “global” stiffness matrix versus elemental  $P$ s shows that the resulting estimates and worst-case estimation errors are in a good agreement.

For the sake of completeness we mention here a variational approach, so called 4DVAR [11], which is based on the maximum likelihood method. That approach minimizes the log-likelihood functional which is equivalent, in the linear case, to a linear quadratic control problem. The solution of the latter is given by the Euler-Lagrange equations in the form of the Pontryagin maximum principle [13], and so it does not require the computation of the operator,  $P$ . Moreover, the resulting estimate at the final time  $T$  coincides with the estimate provided by the Kalman filter. However, 4DVAR type algorithms are not “online”, i.e. one needs to solve a two-point boundary value problem for the Euler-Lagrange equations when the new observation arrives in order to update the estimate. This and the computational complexity of solving the two-point boundary value problem, which, in fact, must be solved iteratively by a so-called shooting method, makes the variational approach quite expensive computationally.

**Experimental assessment** The practical motivation of this work stems from the following problem. For accurate short-term solar energy forecasting (a minute- to hour-ahead) of large geographical areas (continental scale), forecasting models using geostationary operational environmental satellite (GOES) imagery are more effective than numerical weather prediction models as the latter typically takes too long (several hours) to ramp up. The GOES satellite imagery only provides information on the current distribution of clouds, including cloud optical depth (COD) and top/bottom altitude, which can be converted to the current solar irradiance at the surface of the earth using radiative transfer modeling. An accurate cloud advection model is thus required to forecast the future cloud distribution and solar irradiance. We refer the reader to [1] for the further details on this. In section 4 we apply the proposed method for cloud advection over the domain with constant inflow and free-exit boundary condition. The domain spans 16 degrees of longitude and 12 degrees of latitude, and covers approximately 1.68e6 square kilometres.

In addition, we consider a synthetic scenario in which a non-stationary, divergence-free velocity field is advecting a smooth initial data over a domain with non-stationary boundary conditions. We use a relatively low-resolution grid here, as we run the “global filter” for comparison with the “local” filters. One of the experiments suggests that the global filter may become unstable in the case where observations are incomplete as elements with data neighbouring elements without data may give rise to sharp discontinuities, which will appear in  $A$ , and then manifest themselves in  $P$ . This problem is resolved by “moving the discontinuities” off the stiffness matrix (see section 4.1.1). We stress that the proposed method does not face the same type of the instabilities. Finally, we conduct a simple scalability study to demonstrate that the computational cost of the method scales linearly when the number of elements grows (up to  $250 \times 250$ ) and the polynomial order is fixed ( $N = 3$ ) resulting in the discrete state vector of dimension  $10^6$  (see section 4.1.5).

The paper is organized as follows. The problem statement is detailed in section 2, where we describe the advection model and the objectives of the filtering problem. Our main results are in section 3 where we introduce and describe our filtering algorithm. Experimental results for both synthetic and real data are described in section 4, and the conclusions follow in section 5.

**Notation**  $\mathbb{R}^n$  denotes  $n$ -dimensional vector space of real vectors  $\mathbf{x} = (x_1 \dots x_n)^\top$  with standard canonical basis and inner product  $\mathbf{x} \cdot \mathbf{y} = \sum_{j=1}^n x_j y_j$ . Let  $\Gamma$  denote the boundary of the computational domain  $\Omega$ ,  $\Gamma^{in}$  – the inflow zone of  $\Gamma$ , i.e.  $\Gamma^{in} := \{\mathbf{x} \in \Gamma : \mathbf{u}(\mathbf{x}) \cdot \mathbf{n}(\mathbf{x}) < 0\}$ ,  $\mathbf{n}$  is the

unit outward vector which is normal to  $\Gamma$  at  $\mathbf{x}$ , and  $\mathbf{u}(\mathbf{x}) = (u(\mathbf{x}), v(\mathbf{v}))^\top$  is a given incompressible velocity field, i.e.  $\nabla \cdot \mathbf{u} = 0$ . We also set  $\Omega_T := (0, T) \times \Omega$  and  $\Gamma_T^{in}(0, T) \times \Gamma^{in}$  for a real number  $T < +\infty$ . Finally, let  $L^2(\Omega)$  denote the space of square-integrable measurable functions over  $\Omega$ , and let  $H^1(\Omega) := \{f \in L^2(\Omega) : \partial_x f, \partial_y f \in L^2(\Omega)\}$ .

## 2 Problem Statement

The problem we aim to solve is that of state estimation or filtering for a linear advection equation in two spatial dimensions subject to uncertain but bounded error in the initial and boundary conditions, and uncertain forcing. In what follows we introduce the advection equation with uncertain parameters, provide the uncertainty description and formulate the problem statement.

**State equation** Assume that the computational domain  $\Omega \in \mathbb{R}^2$  is a convex bounded domain, and let the function  $(\mathbf{x}, t) \mapsto C(\mathbf{x}, t)$  represent a quantity (e.g. a concentration of a material) which is advected by an incompressible velocity field<sup>1</sup>  $\mathbf{u}$  according to the following linear advection equation:

$$\begin{aligned} \partial_t C(\mathbf{x}, t) + \mathbf{u}(\mathbf{x}) \cdot \nabla C(\mathbf{x}, t) &= b(\mathbf{x}, t)e(\mathbf{x}, t) \text{ in } \Omega_T, \\ C(\mathbf{x}, 0) &= C_0(\mathbf{x}) + b_0(\mathbf{x})e_0(\mathbf{x}), \text{ on } \Omega, \\ C(\mathbf{x}, t) &= C_\partial(\mathbf{x}, t) + b_\partial(\mathbf{x}, t)e_\partial(\mathbf{x}, t), \text{ on } \Gamma_T^{in}, \end{aligned} \quad (3)$$

subject to an uncertain forcing  $e$ , boundary condition  $C_\partial$  and initial condition  $C_0$  with uncertain additive errors  $e_\partial$  and  $e_0$  such that:

$$|q_\partial(\mathbf{x}, t)e_\partial^2(\mathbf{x}, t)| \leq 1, \quad |q_0(\mathbf{x})e_0^2(\mathbf{x})| \leq 1, \quad |q(\mathbf{x}, t)e(\mathbf{x}, t)| \leq 1, \quad (4)$$

provided  $q_0$ ,  $q_\partial$  and  $q$  are given smooth weighting functions such that  $q_0, q_\partial, q > q^* > 0$  for all  $(\mathbf{x}, t) \in \Omega_T$ , and the inequalities are understood for every  $\mathbf{x} \in \Omega$  outside perhaps a set of measure zero. Note that  $q_0$  and  $q$  quantify the level of confidence in the initial condition/boundary conditions and state equation: namely,  $q_0$  may specify “zones” of  $\Omega$  where the knowledge of the initial condition  $C_0$  is more precise or less so, and  $q$  defines zones of  $\Omega$  where (3) holds almost exactly ( $|e| \approx 0$  in that zone) or only up to a significant error ( $|e| > 0$ ) and these zones may vary over time. Statistically, this corresponds to the maximal entropy assumption, i.e., any  $(e_0, e, e_\partial)$  verifying (4) have equal probability of appearing. Functions  $b$ ,  $b_0$  and  $b_\partial$  are assumed to be given and allow one to either localize errors in space/time, or switch them off completely if required.

The equations (3) have a unique smooth solution  $C \in H^1(\Omega_T)$  provided the data in (3), namely  $\mathbf{u}$ ,  $e$ ,  $C_0$ ,  $e_0$ ,  $b$ ,  $b_0$ ,  $b_\partial$  and  $C_\partial$ ,  $e_\partial$  are smooth enough, i.e. of  $H^1(\Omega_T)$  class, and the initial condition agrees with boundary conditions (see [15, p.484]). For the case of less regular solutions, namely just measurable data, the equations (3) still possess the unique weak solution of  $L^2(\Omega_T)$  class (see [2, p.220]), and the discontinuities/steep gradients are propagated forward by the characteristics. For the sake of completeness, we note that the solutions of (3) can receive an even more general representation, namely that of solutions in the space of measures [16] (for the case  $\Omega = \mathbb{R}^n$ ). Since our goal is not in proving the convergence of the proposed method for the most general case, but rather in demonstrating how one can estimate the state of (3) efficiently without compromising much the estimation precision, in what follows, we assume that the data is smooth enough so that  $C$  is at least continuous in  $\mathbf{x}$  and has the classical gradient of  $L^2$ -class.

---

<sup>1</sup>To simplify the presentation we assume that  $\mathbf{u}$  is independent of time so that the inflow part of the boundary  $\Gamma^{in}$  does not change over time. However, in some numerical examples, the proposed method is applied with time-dependent  $\mathbf{u}$ .

**Observation equation** We further assume that a function  $y$  is observed:

$$y(\mathbf{x}_j, t) = C(\mathbf{x}_j, t) + \eta_j(t), \quad j = 1 \dots N_s, \quad (5)$$

where  $\mathbf{x}_j \in \Omega$  denotes the position of a sensor, and a network of  $N_s$ -sensors is deployed in  $\Omega$ . Finally, the observation noise  $\boldsymbol{\eta} := (\eta_1 \dots \eta_{N_s})^\top$  is modelled as a realisation of a vector-valued random process with zero mean and uncertain but bounded correlation function:

$$\int_0^T E(\boldsymbol{\eta}(t) \cdot R^{-1}(t) \boldsymbol{\eta}(t)) dt \leq 1, \quad (6)$$

where  $R(t)$  is a given symmetric positive definite continuous weighting matrix with continuous inverse. This assumption reflects the fact that the second moments of  $\boldsymbol{\eta}$  are known up to a bounded error, e.g. when the moments are estimated by an empirical moment estimator, as often happens in practice.

Finally, let us formulate the problem statement: given state equation (3) together with observations (5) and the uncertainty descriptions (4), (6) our goal is to design an efficient numerical algorithm estimating the quantity  $C(\mathbf{x}, t)$  from  $(y(\mathbf{x}_1, t) \dots y(\mathbf{x}_{N_s}, t))^\top$ .

### 3 Main result

As noted in the introduction, our approach relies upon the “discretize-then-optimize” strategy composed of the following steps:

- 1) the domain,  $\Omega$  is divided into  $K$  of non-overlapping elements,  $D_k$ , and weak formulation of the DG method is applied to (3) on  $D^k$ , namely (3) is substituted by a system of ODEs which describe the evolution (in time) of a vector approximating  $C$  on an element  $D^k$  (section 3.1);
- 2) for each element  $D^k$ , the minimax state estimator is applied to estimate the state of the system of ODEs by using the data localised in  $D^k$ ; the estimators, located at adjacent elements, ‘communicate’ with one another by means of the boundary integral interconnection mechanism of the DG method (section 3.2).

#### 3.1 Discontinuous Galerkin formulation

Applying the DG method to solve the linear advection equation (3) is along the same lines as its application to a general non-linear conservation law. For more details on what follows, see [8]. First, the domain,  $\Omega$  is divided into  $K$  of non-overlapping elements,  $D_k$ , i.e.,  $\Omega \simeq \Omega_h = \bigcup_{k=1}^K D^k$ , where we choose the elements,  $D^k$  to be rectangular. The restriction of the state  $C$  onto the element  $D_k$  is denoted by  $C^k$ . The latter can be approximated by  $C_h^k$ , which is expressed as the series,

$$C_h^k(\mathbf{x}, t) = \sum_{i=1}^{N+1} C^k(\mathbf{x}_i^k, t) \ell_i^k(\mathbf{x}), \quad \mathbf{x} \in D^k, \quad (7)$$

where  $\ell_i^k(\mathbf{x})$  are Lagrange interpolating polynomials in two dimensions defined on points  $\mathbf{x}_i^k$ . These points are taken to be quadrature points for Legendre polynomials, specifically Legendre-Gauss-Lobatto (LGL) points. The series (7) is a nodal expansion representing  $C_h^k$ , i.e.  $C_h^k(\mathbf{x}_i^k, t) = C^k(\mathbf{x}_i^k, t)$ . For more details on this, see [8]. We define  $e_h^k$  and  $e_k^0$ ,  $e_{\partial}^h$ ,  $b_h^k$ ,  $b_{h,0}^k$  and  $b_{h,\partial}^k$  analogously. Substituting  $C_h^k$  into (3), we form the residual  $R_h^k$  on a single element:

$$R_h^k = \partial_t C_h^k(\mathbf{x}, t) + \mathbf{u} \cdot \nabla C_h^k(\mathbf{x}, t) - b_h^k(\mathbf{x}, t) e_h^k(\mathbf{x}, t), \quad \mathbf{x} \in D^k. \quad (8)$$

The Galerkin method involves taking  $\ell_i^k$  as test functions (i.e. same as the expansion/trial functions) and forcing the residual to be orthogonal to each of these test functions. Doing this, and then using integration by parts

$$\int_{D^k} \left( (\mathbf{u} \cdot \nabla C_h^k) \ell_n^k + \nabla \cdot \mathbf{u} C_h^k \ell_n^k + (C_h^k \mathbf{u}) \cdot \nabla \ell_n^k \right) d\mathbf{x} = \int_{\partial D^k} (\hat{\mathbf{n}} \cdot \mathbf{u}) \ell_n^k C_h^k d\mathbf{x},$$

to move the spatial derivatives off the state  $C$  and onto the test functions gives<sup>2</sup> the following weak statement on the element  $D^k$  ( $n = 1 \dots N + 1$ ):

$$\int_{D^k} \left( \partial_t C_h^k \ell_n^k - \mathbf{f}_h^k \cdot \nabla \ell_n^k \right) d\mathbf{x} = - \int_{\partial D^k} \hat{\mathbf{n}} \cdot \mathbf{f}^* \ell_n^k d\mathbf{x} + \int_{D^k} b_h^k e_h^k \ell_n^k d\mathbf{x}, \quad (9)$$

where  $\hat{\mathbf{n}}(\mathbf{x}) = (\hat{n}_x, \hat{n}_y)^\top$  is the unit outward vector which is normal to  $\partial D_k$  at  $\mathbf{x}$ ,  $\mathbf{f}_h^k = (u C_h^k, v C_h^k)^\top$  and  $\mathbf{f}^*$  is the numerical flux function which we take to be the local Lax-Friedrichs flux:

$$\mathbf{f}^*(C_i, C_e, \mathbf{u}_i, \mathbf{u}_e) = \frac{C_i \mathbf{u}_i + C_e \mathbf{u}_e}{2} + \frac{c_s}{2} \hat{\mathbf{n}}(C_i - C_e), \quad (10)$$

where subscripts  $i$  and  $e$  refer respectively to the interior and exterior values at a point on the boundary, and  $c_s$  is the maximum absolute value of the signal speed normal to the boundary at that point, i.e.,

$$c_s = \max\{|\mathbf{u}_i(\mathbf{x}) \cdot \hat{\mathbf{n}}|, |\mathbf{u}_e(\mathbf{x}) \cdot \hat{\mathbf{n}}|\} \quad (11)$$

The surface integral in (9) allows the elements to ‘communicate’ with one another by imposing the values for  $C_h^k$  at the boundary of  $D^k$  from the adjacent elements. In fact, the boundary values are imposed in weak sense [15, p.483] as opposed to the strong/classical sense when the solution takes exactly the prescribed value at the boundary [15, p.482]. This strategy of weak boundary conditions agrees well with our problem statement: indeed, we assume that boundary conditions in (3) are given up to an uncertain function, and so it does make sense to impose boundary conditions “on average” or in the weak sense. Since we are using rectangular elements, the surface integral is just the sum of four line integrals, each one over one face of the element  $D^k$ . The exterior solution values  $C_e$  in (10) and (11) refer to the value of  $C_h^k$  at  $\mathbf{x}$  at the boundary of a neighbouring element which shares the boundary with  $D^k$ . If  $\mathbf{x}$  belongs to the physical boundary of the domain,  $\Gamma$ , the exterior value is determined by the third equation of (3). More specifically, if the flow direction at  $\mathbf{x}$  is ‘into’ the domain, i.e.  $\hat{\mathbf{n}}(\mathbf{x}) \cdot \mathbf{u}(\mathbf{x}) < 0$ , then  $C_e$  is set to either the value of  $C_h^k$  at  $\mathbf{x}$  at the boundary of a neighbouring element or the value prescribed by the 2nd equation of (3). If, on the other hand, the flow direction at that boundary point is ‘out of’ the domain (i.e.  $\hat{\mathbf{n}}(\mathbf{x}) \cdot \mathbf{u}(\mathbf{x}) > 0$ ), then a free exit boundary condition is imposed at that point by setting  $C_e$  equal to the interior value  $C_i$ . Note that the Lax-Friedrichs numerical flux adds artificial viscosity at the element interfaces in its handling of the jump in state,  $C_i - C_e$ . This smooths discontinuities which may occur at those interfaces.

The weak DG formulation of (3) on a single element  $D^k$  can be written as:

$$M^k \frac{d\mathbf{C}_h^k}{dt} - S_x^\top \mathbf{F}_x - S_y^\top \mathbf{F}_y = - \sum_{i=1}^4 (-1)^i M_e^{k,i} \mathbf{F}_i^* + M^k B^k(t) \mathbf{e}^k(t), \quad (12)$$

$$\mathbf{C}_h^k(0) = \mathbf{C}_0^k + B_0^k \mathbf{e}_0^k,$$

where  $M^k$ ,  $S_x$  and  $S_y$  are the mass and stiffness matrices with the latter corresponding to advection in the  $x$ - and  $y$ -directions<sup>3</sup>. The vectors  $\mathbf{C}_h^k$ ,  $\mathbf{C}_0^k$ ,  $\mathbf{e}^k$  and  $\mathbf{e}_0^k$  are grid-functions representing  $C_h^k$ ,

<sup>2</sup>Recall that  $\nabla \cdot \mathbf{u} = 0$ .

<sup>3</sup>See appendix A for the derivation of the mass and stiffness matrices.

$C_0, e_0, e$  respectively on the  $(N+1)^2$  LGL quadrature points of the element  $D^k$ , and the vectors  $\mathbf{F}_x$  and  $\mathbf{F}_y$  are grid functions representing the first and second components of  $\mathbf{f}_h^k$  respectively.  $B^k$  and  $B_0^k$  are diagonal matrices with the grid-functions  $\mathbf{b}_h^k$  and  $\mathbf{b}_{h,0}^k$  on the diagonal respectively. The matrices  $M_e^{k,i}$  are *edge-mass* matrices for the element  $D^k$  on face  $i$ , where the faces,  $i = 1 \dots 4$ , are ordered: *left, right, lower, upper*. These matrices act on the vector  $\mathbf{F}_i^*$  which is a grid function representing the numerical flux, (10), over each node on face  $i$ .

As noted above, the weak DG formulation of (3) on a single element  $D^k$  leads to the ODE (12) which describes the time evolution of the vector  $\mathbf{C}_h^k$ , the grid-function representing  $C_h^k$  on the  $(N+1)^2$  LGL quadrature points on element  $D^k$ . The source term  $\mathbf{F}_i^*$  of (12) depends upon vectors  $\mathbf{C}_h^s$ ,  $s \neq k$  which approximate  $C_h^s$  on  $D^s$ . It is responsible for the “exchange of information” between the “local” approximations of  $C_h^s$ . This “communication mechanism” plays an important role in the distributed filtering algorithm presented in section 3.2.

### 3.2 Distributed minimax filter

To proceed we first transform (12) into a form suitable for the application of the minimax state estimator. We introduce an affine transformation:

$$\begin{aligned} A^k(t)\mathbf{C}_h^k(t) + \mathbf{B}^k(t, \mathbf{C}_h^s) + W^k \mathbf{e}_\partial^k(t) &:= (M^k)^{-1} (S_x^\top \mathbf{F}_x(t) + S_y^\top \mathbf{F}_y(t)) \\ &\quad - (M^k)^{-1} \sum_{i=1}^4 (-1)^i M_e^{k,i} \mathbf{F}_i^*(t) \end{aligned} \quad (13)$$

where the first term on the right hand side accounts for the advection of the state quantity,  $\mathbf{C}_h^k$  within the element  $D^k$  in the absence of boundary effects, and the second term accounts for inter-element boundary fluxes. Of those two terms, the first is linear in  $\mathbf{C}_h^k$ , as is clear from the definitions of  $M^k$ ,  $S_x$ ,  $S_y$  in appendix A, and of  $\mathbf{F}_x$  and  $\mathbf{F}_y$  in section 3.1. The second term, however is affine in  $\mathbf{C}_h^k$ , which we can see if we look at the numerical flux given by (10) which is approximated by the grid-function,  $\mathbf{F}_i^*$  above. The interior state,  $C_i$ , in that equation is approximated by  $\mathbf{C}_h^k$  restricted to the nodes on the appropriate boundary. However, the other terms in that equation do not depend on  $\mathbf{C}_h^k$  so are treated as an external source term. As a result, in addition to containing the stiffness terms,  $A^k \mathbf{C}_h^k$  also absorbs part of the flux term, while  $\mathbf{B}^k$  represents only the component of the flux that depends on the state  $\mathbf{C}_h^s$  on elements  $D^s$  neighbouring  $D^k$ . Finally,  $\mathbf{e}_\partial^k$  represents the component of the flux that depends on  $e_\partial$  which is only the case when  $D^k \cap \Gamma^{in} \neq \emptyset$ . The term  $\mathbf{e}_\partial^k$  is in effect a flux term induced by the error at the physical boundary, i.e.,  $\mathbf{e}_\partial^k = -(M^k)^{-1} \sum_{i=1}^4 (-1)^i M_e^{k,i} \mathbf{F}_\partial^*(t)$  where  $\mathbf{F}_\partial^*(t)$  is a grid-function approximating the Lax-Friedrichs flux, (10), with external state,  $C_e = e_\partial$ . The matrix,  $W^k$  restricts  $\mathbf{e}_\partial$  to the boundary  $D^k$  when  $D^k$  has a boundary which intersects with  $\Gamma$ , otherwise  $W^k$  is zero. Note that the effect of  $C_\partial$  is absorbed by  $\mathbf{B}^k$ . In other words,  $\mathbf{B}^k$  represents the “known” part of the boundary conditions (either from  $\partial D^k$  or from  $\Gamma^{in}$ ), and  $\mathbf{e}_\partial^k$  accounts for the uncertain part of the boundary conditions coming from  $e_\partial$ . In what follows we will refer to  $A^k$  as the state transition matrix, or system matrix for short. Having said this, we can rewrite (12) as follows:

$$\frac{d\mathbf{C}_h^k}{dt} = A^k(t)\mathbf{C}_h^k + \mathbf{B}^k(t, \mathbf{C}_h^s) + V^k \tilde{\mathbf{e}}^k(t), \quad \mathbf{C}_h^k(0) = \mathbf{C}_0^k + B_0^k \mathbf{e}_0^k. \quad (14)$$

where  $V^k := (B^k \ W^k)$  and  $\tilde{\mathbf{e}}^k = (\mathbf{e}^k, \mathbf{e}_\partial^k)^\top$ . Note that  $B^k = 0$ ,  $W^k = 0$  provided  $b = 0$  and  $b_\partial = 0$  respectively.

Now, let us introduce a bounding set for the uncertain vectors  $\mathbf{e}_0^k$  and  $\tilde{\mathbf{e}}^k$ . We recall that  $\mathbf{e}_0^k = (C_0(\mathbf{x}_1^k \dots C_0(\mathbf{x}_{(N+1)^2}^k))^\top$ , and  $\mathbf{e}^k, \mathbf{e}_\partial^k$  are defined analogously. Define  $Q_0^k := \text{diag}(q_0(\mathbf{x}_1^k) \dots q_0(\mathbf{x}_{(N+1)^2}^k))$ ,



the restriction of  $q_0$  onto the LGL grid of  $D^k$ . Let  $Q^k(t)$  denote the restriction of  $q$  onto the LGL grid, defined in the same way. Let  $Q_\partial^k(t)$  denote the restriction of  $q_\partial$  onto the LGL grid points located at the boundary of  $D^k$ . Since  $q_0, q_\partial, q > q^* > 0$ , it follows that  $Q_0^k, Q_\partial^k$  and  $Q^k$  are positive definite. By (4), we get that

$$\mathbf{e}_0^k \cdot Q_0^k \mathbf{e}_0^k + \int_t^{t+s} (\tilde{\mathbf{e}}^k(\tau) \cdot \tilde{Q}^k(\tau) \tilde{\mathbf{e}}^k(\tau)) d\tau \leq (1 + 2s)(N + 1)^2, \quad (15)$$

provided  $\tilde{Q}^k := \text{diag}(Q^k, Q_\partial)$ . This approximation represents an ellipsoid containing  $\mathcal{C}^k$ , the restriction of the hypercube defined by (4) onto the LGL grid within  $D^k$ . Clearly, the aforementioned ellipsoid “contains more uncertainty” than the restricted hypercube  $\mathcal{C}^k$ : indeed, this is indicated by the presence of the factor  $(N + 1)^2$ . However, in practice,  $N$  (the degree of Lagrange polynomials) is typically not taken to be higher than the low integers. The numerical precision of the DG method is increased by fixing  $N$  and refining the partition of  $\Omega$  by introducing more elements  $D^k$  of smaller area. For example, we used  $N = 3$  and  $70 \times 70$  rectangular partition of  $\Omega$  to advect a satellite image of the cloud optical depth (see section 4.2). Therefore, the factor  $(N + 1)^2$  has a positive effect (at least for  $N \leq 5$ ) as it allows one to provide a slightly more conservative uncertainty description in the form (15) which accounts for discretization errors as well as for the model errors making the resulting state estimate more robust by increasing the worst-case estimation error (see proposition 1).

Finally, we recall that a network of  $N_s$ -sensors is deployed in  $\Omega$ . We denote by  $D_{obs}^k := \{\mathbf{x}_{j_1} \dots \mathbf{x}_{j_{M_k}}\}$  the locations of the sensors which belong to  $D^k$  and define

$$\mathbf{Y}^k = (y(\mathbf{x}_{j_1}, t) \dots y(\mathbf{x}_{j_{M_k}}, t))^\top \quad H^k = \{\ell_n^k(\mathbf{x}_{j_{M_k}})\}_{n,j=1}^{M_k, (N+1)^2}$$

the restriction of  $y$  defined by (5) onto  $D_{obs}^k$ , and the interpolation matrix  $H^k$  mapping LGL grid to  $D_{obs}^k$ . Similarly, we define  $\boldsymbol{\eta}^k = (\eta_{j_1} \dots \eta_{j_{M_k}})^\top$ , the restriction of the observation noise onto the element  $D^k$ . Let  $\pi$  denote a matrix of norm 1 mapping  $\boldsymbol{\eta}$  to  $\boldsymbol{\eta}^k$ , and define  $R^k := \pi^\top R \pi$ . If  $D^k$  does not contain a single sensor we set<sup>4</sup>  $H^k := 0$ . As a result, the observations take the following form:

$$\mathbf{Y}^k = H^k \mathbf{C}_h^k(t) + \boldsymbol{\eta}^k,$$

Now, following [22] we state the following proposition:

**Proposition 1.** *Assume that  $\mathbf{C}^k$  solves (14) and the uncertain parameters are bounded according to (15). Given observations  $\mathbf{Y}^k$  we define the minimax estimate  $\hat{\mathbf{C}}_h^k$  on  $D^k$  as follows:*

$$\frac{dP^k}{dt} = A^k P^k + P^k (A^k)^\top + V^k (\tilde{Q}^k)^{-1} (V^k)^\top \quad (16)$$

$$- P^k (H^k)^\top (R^k)^{-1} H^k P^k, \quad P^k(t) = P_{prev}^k(t), \quad (17)$$

$$\frac{d\hat{\mathbf{C}}_h^k}{dt} = A^k \hat{\mathbf{C}}_h^k + \mathbf{B}^k(t, \hat{\mathbf{C}}_h^s) \quad (18)$$

$$+ P^k (H^k)^\top (R^k)^{-1} (\mathbf{Y}^k - H^k \hat{\mathbf{C}}_h^k), \quad \hat{\mathbf{C}}_h^k(0) = \mathbf{C}_0^k \quad (19)$$

where  $\hat{\mathbf{C}}_h^s$  is the minimax estimate on elements  $D^s$  neighbouring  $D^k$ . It then follows that

$$\max_{\tilde{\mathbf{e}}^k, \mathbf{e}_0^k, E\boldsymbol{\eta}^k(\boldsymbol{\eta}^k)^\top} E(\mathbf{C}_h^k(\mathbf{x}_j, t + s) - \hat{\mathbf{C}}_h^k(\mathbf{x}_j, t + s))^2 = (1 + 2s)(N + 1)^2 P_{jj}(t + s), \quad (20)$$

<sup>4</sup>It will become apparent after Proposition proposition 1 that setting  $H^k = 0$  is mathematically equivalent to the “no observation” case: indeed, the state estimator is coupled to  $\mathbf{Y}^k$  by means of  $H^k$  so this coupling becomes trivial if  $H^k = 0$  and the state estimator reduced to the state equation (14) with no uncertainty, e.g.  $\mathbf{e}_\partial = 0$ ,  $\mathbf{e}_0^k = 0$  and  $\mathbf{e}^k = 0$ .

i.e. the worst-case mean-squared error of the minimax estimate  $\hat{C}_h^k(\mathbf{x}_j, t + \delta t)$  of the value  $C_h^k(\mathbf{x}_j, t + \delta t)$  is given by the  $j$ th diagonal element of the unique symmetric positive definite solution of the Riccati equation (16)-(17).

The proof of the proposition is given in appendix B. Note that proposition 1 reflects the sequential nature of the estimation process: at  $t = 0$  we initialize the process by setting  $P_{prev}^k(0) := B_0^k(Q_0^k)^{-1}B_0^k$ , which describes the a priori bound for the initial condition error, and compute  $P^k$  and  $\hat{C}_h^k$  on  $(0, s)$  by solving (16)-(19);  $t$  is then set to  $s$ ,  $P_{prev}(t)$  is set to  $P^k(t)$  and (16)-(19) is solved again on  $(t, t + s)$ . The factor  $(1 + 2s)(N + 1)^2$  in (20) comes from the ellipsoidal approximation of the discretized hypercubes (4), which is required to formulate the minimax filter [20]. As a result, the mean-squared worst-case estimation error is inflated after each estimation step at  $t + s$  by the constant factor  $(1 + 2s)(N + 1)^2$  so that at time  $T$  the estimation error is given by  $(1 + 2T)(N + 1)^2 P_{jj}$ . We stress that the equation for  $P^k$  is composed of the following parts:

- the linear part (16) represents Lyapunov operator which describes dynamics of the estimation error in the absence of observations (e.g.  $H^k = 0$ ),
- the nonlinear part (17) represents the reduction in the estimation error due to observations.

Similarly, the state estimator equations consists of the model (18) and the innovation part (19). Both (17) and (19) disappear if  $D^k$  does not contain a single sensor.

We stress that the gain  $P^k$  does not depend on the gains  $P^s$  at the neighbouring elements. In contrast, the minimax estimates  $\hat{C}_h^k$  at elements  $D^k$  are advanced independently over the time window  $[t, t + s]$ , and the communication terms  $B^k(t, \hat{C}_h^s)$  are updated at  $t + s$ . In this way, the filters on elements with no observations receive information from the elements with observations, so that the localised observations are, in fact, spread around the entire domain due to the communication terms  $B^k(t, \hat{C}_h^s)$ .

### 3.3 Time discretisation

It was noted in [21] that equations (16)-(19) must be discretized by a method (e.g. symplectic Runge-Kutta method of order  $p$ ) preserving quadratic invariants of the estimation error dynamics, i.e. the discrete estimate should verify the equality (20). The latter holds true for the symplectic Mobius integrator proposed in [6] to solve the matrix differential Riccati equation (16). The basic idea behind the Mobius transformation is to make use of the fact that the solution of the Riccati equation induces a flow on a Grassmannian manifold. This flow is called a Mobius transformation. It may be constructed by solving an associated linear Hamiltonian system: indeed, the solution of the Riccati equation,  $P^k$ , can be expressed in the form  $P^k = V^k(U^k)^{-1}$  provided

$$\begin{pmatrix} \dot{U}^k \\ \dot{V}^k \end{pmatrix} = \begin{pmatrix} -A^{k\top} & (H^k)^\top (R^k)^{-1} H_k \\ \bar{Q}_k & A^k \end{pmatrix} \begin{pmatrix} U^k(t) \\ V^k(t) \end{pmatrix}, \quad \begin{pmatrix} U^k(t) \\ V^k(t) \end{pmatrix} = \begin{pmatrix} I \\ P^k(t) \end{pmatrix} \quad (21)$$

where  $\bar{Q}_k := (1 + 2s)(N + 1)^2 V^k \tilde{Q}^k (V^k)^{-1}$ , and the initial gain,  $P^k(0) := (1 + 2s)(N + 1)^2 B_0^k (Q_0^k)^{-1} B_0^k$ . The Hamiltonian system (21) can be solved by using symplectic Runge-Kutta methods of order 2 and thus avoid numerical instabilities associated with Mobius transform by means of a reinitialization: namely the gain at time level  $j + 1$  is given by  $P_{j+1}^k = V_{j+1}^k (U_{j+1}^k)^{-1}$  provided

$$\begin{aligned} & \begin{pmatrix} I + \frac{\Delta T}{2} (A_j^k)^\top & -\frac{\Delta T}{2} (H^k)^\top (R_{j+1}^k)^{-1} H_k \\ -\frac{\Delta T}{2} (\bar{Q}^k)^{-1} & I - \frac{\Delta T}{2} A_j^k \end{pmatrix} \begin{pmatrix} U_{j+1}^k \\ V_{j+1}^k \end{pmatrix} \\ &= \begin{pmatrix} I - \frac{\Delta T}{2} (A_j^k)^\top & \frac{\Delta T}{2} (H^k)^\top (R_j^k)^{-1} H_k \\ \frac{\Delta T}{2} (\bar{Q}^k)^{-1} & I + \frac{\Delta T}{2} A_j^k \end{pmatrix} \begin{pmatrix} I \\ P_j^k \end{pmatrix} \end{aligned} \quad (22)$$

where  $\Delta T$  is the time-step, and  $s := \Delta T$ . The reinitialization is in that  $U_j^k$  is set to the identity matrix and  $V_j^k = P_j^k$  so that  $(U_{j+1}^k)^{-1}$  is well-conditioned. The resulting symplectic Mobius integrator (22) is stable and preserves symmetry and positivity of the Riccati matrix. Also it preserves all quadratic invariants of the estimation error dynamics including (20). Finally, the filter equation in (18)-(19) is also solved using the implicit midpoint method, giving:

$$\begin{aligned} & \left( I - \frac{\Delta T}{2} A_{j+1}^k + \frac{\Delta T}{2} P_{j+1}^k (H^k)^\top (R_{j+1}^k)^{-1} H_k \right) (\hat{C}_h^k)_{j+1} = \Delta T B_j^k \\ & \left( I + \frac{\Delta T}{2} A_j^k - \frac{\Delta T}{2} P_j^k (H^k)^\top (R_j^k)^{-1} H_k \right) (\hat{C}_h^k)_j \\ & + \frac{\Delta T}{2} \left( \frac{P_{j+1}^k (H^k)^\top (R_{j+1}^k)^{-1} \mathbf{Y}_{j+1}^k + P_j^k (H^k)^\top (R_j^k)^{-1} \mathbf{Y}_j^k}{2} \right), \end{aligned} \quad (23)$$

Note that the above scheme is explicit in  $B_j^k$  as at time level  $j$  we only have  $B_j^k$ .

### 3.4 Varying trust in observations

When filtering, the amount of trust placed in the observations,  $\mathbf{Y}^k$ , is regulated by the symmetric positive definite matrix,  $R^k$ : small eigenvalues of  $R$  represent high trust and the reverse. Intuitively, low trust (high eigenvalues) reduces the “rate” at which local filter assimilates the observations by reducing the impact of the innovation term (19). This simple fact is used to assimilate sparse in time observations in a stable fashion. Indeed, if the observations are available at discrete time instants, i.e. the matrix  $H^k$  switches between 0 and identity matrix, the numerical scheme (18)-(19) could quickly become unstable due to the hyperbolic nature of the problem (3). To overcome this, we suggest the following procedure: instead of switching  $H^k$  between 0 and 1 to mimic the presence/absence of the observations, we fix  $H^k$  and vary the trust in  $\mathbf{Y}^k$  by multiplying  $R^k$  by a scalar  $r^k > 0$  which dictates the trust placed in the observations associated with element  $k$ . Small  $r^k$  indicates high trust, while large  $r^k$  indicates low trust. More specifically, the algorithm assumes that no data are available at  $t = 0$ , so  $r^k$  is initialised to a high value. When observations become available, say at  $t = t_1$ , then  $r^k$  should be decreased from its default high value to a low value in order to increase the trust in the observations for element  $k$ . However, sharply decreasing  $r^k$  can cause the system to become numerically unstable, so instead of doing this, we reduce its value over time, thus increasing the trust gradually and avoiding instabilities. The observations should however be assimilated relatively fast to avoid lag, so reducing  $r^k$  at each computational time-step would not be ideal unless  $\Delta T$  was set to a small value (i.e. smaller than necessary to ensure numerical stability of the scheme). This, however, would be computationally inefficient so instead, we introduce a second, smaller time-step,  $\Delta T_s$ , where  $n_s \Delta T_s = \Delta T$ , so that when data become available, we can switch to using the smaller time-step,  $\Delta T_s$ , running the filter  $n_s$  times over  $[t_1, t_1 + \Delta T]$  while varying  $r^k$  over that time-interval. The trust at the beginning of the time interval is small (high  $r^k$ ) and should also be small at the end. Thus, we vary  $r^k$  in such a way that it attains a specific minimum value associated with high trust mid-way through the time interval. We achieve this by reducing  $r^k$  for the first  $n_s/2$  small time-steps (setting  $n_s$  to be even) and then increasing it back to a high value over the remaining  $n_s/2$  steps. This procedure resembles the (weak) approximation of the Dirac delta-function by Gaussian densities.

The distributed filtering algorithm is summarised as algorithm 1, where we use the following notation:

- $\Delta T$ : Standard computational time-step

- $N_t$ : Number of standard time-steps
- $N_c$ : Number of time-steps used at current time-level
- $n_s$ : Number of small time-steps for filtering (even)
- $K$ : Number of DG elements
- $\Delta T_c$ : Time-step at current time-level
- $E_s$ : Set of DG elements on which observations may be available
- $r^k$ : Observation trust parameter
- $r_{tr}$ : High trust value of  $r^k$
- $r_d$ : Low trust value of  $r^k$
- $\tau$ : Constant for varying trust, where  $r_d \tau^{-n_s/2} = r_{tr}$

Note that there are two nested time-loops in algorithm 1. For the outer loop (using control variable,  $i$ ) time is advanced using the standard computational time-step,  $\Delta T$ , and for the inner one (using control variable,  $j$ ) time is either incremented by the standard computational time-step for a single iteration in the case that no observations are available, or by the small time-step,  $\Delta T_s$  for  $n_s$  iterations when observations are available on any element. The time,  $t$ , set inside the outer loop is the time at the beginning of the current time-level. It is at this time that a check is performed for available observations. Inside the inner time-loop,  $t$  is then updated to be the estimate/solution time. This will be either  $\Delta T$  or  $\Delta T_s$  beyond the time at the beginning of the current time-level, depending on whether or not observations are available.

Note also that the loop over DG elements (using control variable,  $k$ ) can be easily parallelised as it is called within the inner time-loop and hence runs over a single time-level at a time. As a result, the elemental estimates/solutions can be obtained in any order, since (22) and (23) form a two-level scheme whereby the solution at the current time-level is obtained using the solution at the previous level.

## 4 Numerical Experiments

In this section, we describe numerical experiments in both synthetic and real scenarios. The real scenario is that of cloud motion where we use a sequence of velocity fields which are obtained using an optical flow estimation procedure. The observations we use are satellite images depicting cloud optical depth. We employ the distributed filter here on a high-resolution grid on a domain with constant inflow and free-exit boundary conditions.

The synthetic scenario uses a non-stationary, divergence-free velocity field to advect smooth initial data over a domain with non-stationary boundary conditions. We use a relatively low-resolution grid here, as we run the global filter for comparison with the distributed filter on this test-case, with the former being more computationally expensive. The grid resolution required for the real data would be too expensive for the global filter.

---

**Algorithm 1** Distributed filtering for 2D advection

---

```

 $r^k \leftarrow r_d$ 
for  $i = 1$  to  $N_t$  do
   $t \leftarrow (i - 1)\Delta T$ 
  if Observations are available on any element at time,  $t$  then
     $N_c \leftarrow n_s$ 
     $\Delta T_c \leftarrow \Delta T/n_s$ 
  else
     $N_c \leftarrow 1$ 
     $\Delta T_c \leftarrow \Delta T$ 
  end if
  for  $j = 1$  to  $N_c$  do
     $t \leftarrow t + j\Delta T_c$ 
    Update boundary conditions and advection field for time  $t$ 
    for  $k = 1$  to  $K$  do
      Compute elemental system matrix,  $A^k$ , and vector,  $\mathbf{B}^k$ 
      if Element  $k \in E_s$  then
        Filter: Compute gain,  $P^k$ , and estimate,  $\hat{\mathbf{C}}_h^k(t)$ , using (22) and (23) with current
        time-step,  $\Delta T_c$ 
        if  $N_c = n_s$  then
          Vary trust in observations:
          if  $j \leq n_s/2$  then
             $r^k \leftarrow r^k/\tau$ 
          else
             $r^k \leftarrow r^k\tau$ 
          end if
        end if
      end if
    else
      Solve forward: Set  $H^k = 0$  and compute  $P^k$  and  $\hat{\mathbf{C}}_h^k$ , using (22) and (23)
    end if
  end for
  Assemble full estimate  $\hat{\mathbf{C}}_h(t)$  at time  $t$  by combining all  $K$  elemental estimates  $\hat{\mathbf{C}}_h^k(t)$ 
end for
end for

```

---

## 4.1 Assimilation of synthetic data

The distributed filter is first tested on the domain,  $\Omega = [0, 2\pi] \times [0, 2\pi]$ , discretised into a  $10 \times 10$  element grid with  $N = 3$ . We first generate synthetic observations by solving the advection equation, (3), using the implicit midpoint method with time-step,  $\Delta T$ , over  $t \in [0, T]$  with initial data,

$$C(\mathbf{x}, 0) = \sin(x) \cos(y) + 1.2, \quad \mathbf{x} = (x, y)^\top \in \Omega \quad (24)$$

with the divergence-free velocity-field,

$$\mathbf{u}(\mathbf{x}, t) = \begin{pmatrix} u \\ v \end{pmatrix} = \begin{pmatrix} \sin(\frac{x}{2}) \sin(\frac{y}{2}) \cos(\frac{2\pi t}{10}) \\ \cos(\frac{x}{2}) \cos(\frac{y}{2}) \cos(\frac{2\pi t}{10}) \end{pmatrix} \quad (25)$$

and boundary conditions,

$$\begin{aligned} C_{lower}(x, t) &= C_{upper}(x, t) = \sin(x) \cos(t), \quad x \in [0, 2\pi], \\ C_{left}(y, t) &= C_{right}(y, t) = \sin(y) \cos(t), \quad y \in [0, 2\pi]. \end{aligned} \quad (26)$$

The numerical solution,  $C(\mathbf{x}_j, t)$ ,  $t \in [\Delta T, T]$  is used as observations, i.e.  $y(\mathbf{x}_j, t) = C(\mathbf{x}_j, t) + \eta_j(t)$  with 1% of the signal-to-noise ratio, which is reflected by  $r^{tr} = 1e - 5$  in the matrix  $R = r^{tr} I$ . We set  $\mathbf{Y}_s(t) := \{y(\mathbf{x}_j, t)\}_{j=1}^{(N+1)^2 K}$  and use this vector-function for the tests in the synthetic scenario.

### 4.1.1 Global filter

For the case of synthetic model parameters and observations, we compare the results of the distributed filter to the global implementation. This involves filtering using a single global system of equations as opposed to  $K$  elemental systems. For this comparison we assume that there is no model error, and boundary conditions are known too, so that  $b = 0$  and  $b_\partial = 0$ . The global DG system in this case can be written as

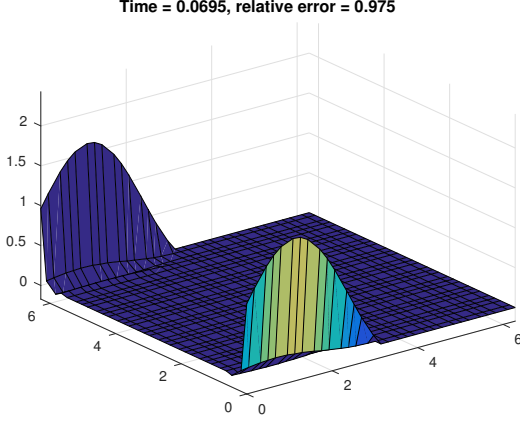
$$\frac{d\mathbf{C}_h}{dt} = A\mathbf{C}_h + \mathbf{B}, \quad \mathbf{C}_h(0) = \mathbf{C}_0 + \mathbf{e}_0^g, \quad (27)$$

where  $A$  is a global system matrix and  $\mathbf{B}$  is a global flux vector. The filter equations are the same as those in section 3.2, except with global terms in place of local. An apparent advantage of this approach is that unlike in the local formulation, the system matrix,  $A$ , absorbs the entire inter-element flux term (rhs of (12)) except in the case where the element boundary in question lies on the domain boundary,  $\Gamma$ . In that case, the terms in (10) which come from the boundary data contribute to vector,  $\mathbf{B}$ . As a result, that flux vector only contains information relating to the domain boundary, while the global matrix,  $A$  absorbs everything else. The advantage of this approach is that the global gain,  $P$  is informed by richer information than is  $P_k$  in the distributed case. However, in the case where observations are incomplete, elements with data neighbouring elements without data may give rise to sharp discontinuities, which will appear in  $A$ , and then manifest themselves in  $P$ . In anticipation of this issue, we can form another global system,

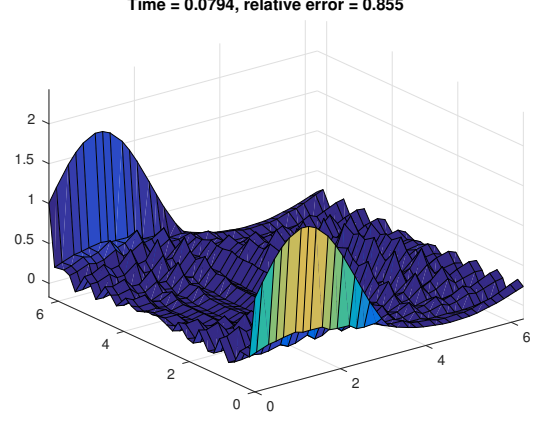
$$\frac{d\mathbf{C}_h}{dt} = A_b\mathbf{C}_h + \mathbf{B}_b, \quad \mathbf{C}_h(0) = \mathbf{C}_0 + \mathbf{e}_0^g, \quad (28)$$

where for the range of rows of  $A_b$  relating to a given element,  $k$ , terms containing the state outside of that element are placed in  $\mathbf{B}_b$ . Using this approach, discontinuities due to spatially sparse observations will not appear in  $A_b$  and hence neither in the gain,  $P$ . The gain will now be fed by the same information as in the case of the distributed filter where a similar approach was taken by necessity. The trust in the observations is varied in the same way in the global case as it is for the distributed filter described in section 3.4.

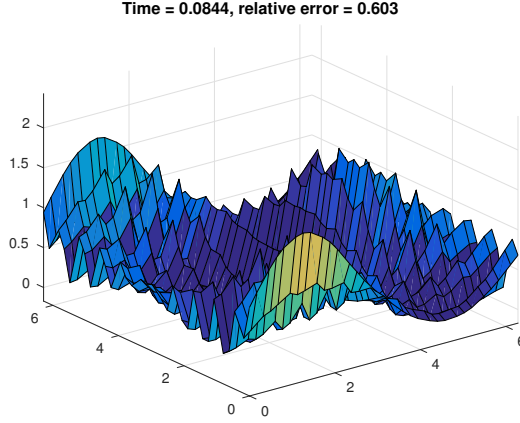
Later, we compare the cost of the global filter to that of the distributed filter.



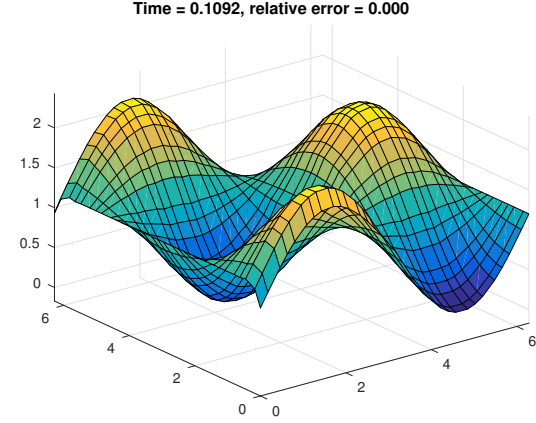
(a) Estimate at  $t = \Delta T$ : influenced only by initial and boundary conditions



(b) Estimate at  $t = 0.0794$ : assimilating observation



(c) Estimate at  $t = 0.0844$ : assimilating observation



(d) Estimate at  $t = 0.1092$ : assimilated observation

Figure 1: Assimilation of a single full observation with precise boundary conditions and velocity field (Synthetic Test 1)

#### 4.1.2 Synthetic Test 1: Full observations over time and space

In the first test, we initialise the filter to zero, i.e.,  $\mathbf{C}_0(\mathbf{x}) = 0$ , and impose the correct boundary conditions, (26), and velocity field, (25), while taking a single observation over all LGL points at one computational time-level ( $t = \Delta T$ ), where the time step  $\Delta T$  is the same for the filter as it is for the forward run for generating observations. We thus set  $b = 0$  (no model error),  $b_0 = \frac{1}{\sqrt{8}}$  (rescaled initial condition error) and  $b_\partial = 0$  (exact boundary conditions). As a result,  $V^k = 0$  in (16)- (19). We also set  $q_0 = \frac{1}{2}$  so that  $P^k(0) = (1 + 2\Delta T)(N + 1)^2 B_0^k (Q_0^k)^{-1} B_0^k \approx I$  indicating small trust to the initial conditions. Note, that the minimax filter does not depend on initial conditions, provided it is integrated for a long enough time that  $P^k(0)$  is forgotten.

This is a simple experiment to observe how the filter reacts to the incorrect initial condition. The time-evolution of the distributed filter for  $t \in [0, 0.1092]$  is shown in figure fig. 1. The error shown in the figures is the relative  $L^2$  error, i.e.  $\|\mathbf{Y}(t) - \hat{\mathbf{C}}_h(t)\| / \|\mathbf{Y}(t)\|$ . The computational time-step,  $\Delta T = 0.0695$  and the filtering time-step,  $\Delta T_s = \Delta T/14$  meaning we run the filter with varying trust 14 times over  $t \in [\Delta T, 2\Delta T]$  for the observation,  $\mathbf{Y}_s(\Delta T)$ , which becomes available at  $t = \Delta T$  (see section 3.4 and algorithm 1). Until  $t = \Delta T$ , the estimate is zero everywhere apart

from at the regions affected by the boundary conditions, which may elicit an inflow depending on the direction of the velocity field on the boundaries (see section 3.1). We see this in fig. 1a, where observations have not yet become available. In fig. 1b, the first observation is being assimilated at time  $t = \Delta T + 2\Delta T_s$ , i.e., the 2nd time-step of the inner time-loop in algorithm 1. By  $t = 0.1092$ , the first observation has been assimilated and the relative error is  $\approx 1e - 4$ . This is then compared to the result of the global filter with fully global system matrix,  $A$ , and boundary flux vector,  $B$  (see (27)), as described in section 4.1.1, under the same conditions. The relative errors for both the local and global filters over time are shown in fig. 2, where the observation becomes available at  $t = \Delta T$ . At  $t = 0.1092$  (i.e,  $t = \Delta T + 8\Delta T_s$ ), the relative error in the global case is also  $\approx 1e - 4$ .

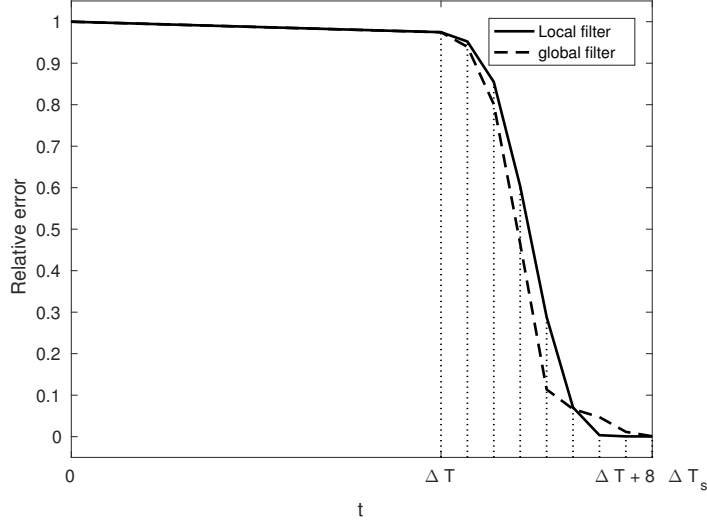
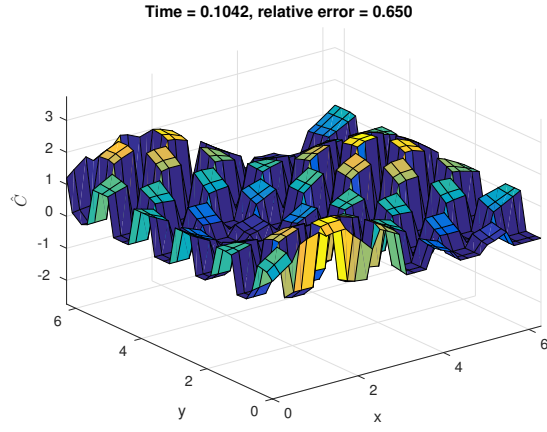


Figure 2: Estimate error for local and global filters for 1 full observation with precise boundary conditions and velocity field (Synthetic Test 1)

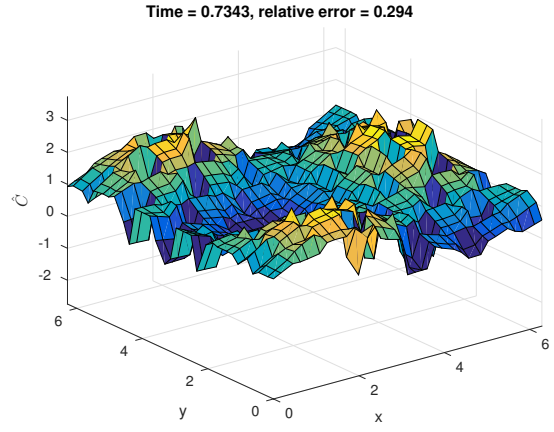
#### 4.1.3 Synthetic Test 2: Sparse observations in space

In the second test, we provide the filter with the correct boundary conditions, (26), and velocity field, (25), but incomplete observations. Specifically, we equip every other element with observations in a “chequered” pattern. This experiment is designed to test the filter in the presence of discontinuities in the observations which may occur when dealing with sparse data. Like in the previous experiment, the estimate is initialised to zero, while observations are available at times,  $t = \Delta T, 2\Delta T, \dots$ . We use the same  $b$ ,  $b_0$ ,  $b_\partial$  and  $q_0$ . The time-evolution of the estimate is shown in fig. 3. We see the first observation being assimilated in fig. 3a where the “chequered” observation pattern is apparent. The subsequent figures show the estimate as further observations are assimilated; we see that over time, the observation pattern becomes less apparent as the velocity field induces a flux between neighbouring elements, and the relative error decreases over time. We repeat the same test with the global filter on the system, (27), for comparison. This fails to converge, as we see from fig. 4a. As discussed in section 4.1.1, discontinuities generated by sparse observations will manifest themselves in the global gain, possibly leading to instabilities. This could account for the failure of the global filter in this case. We re-attempt the experiment with the system, (28), where the system matrix,  $A_b$ , and flux vector,  $B_b$ , are described in section 4.1.1. To summarise that discussion, the system matrix is not fully global, as for a given element, components of the state on neighbouring elements are placed in the flux vector,  $B_b$  instead of in  $A_b$ . As a result, the

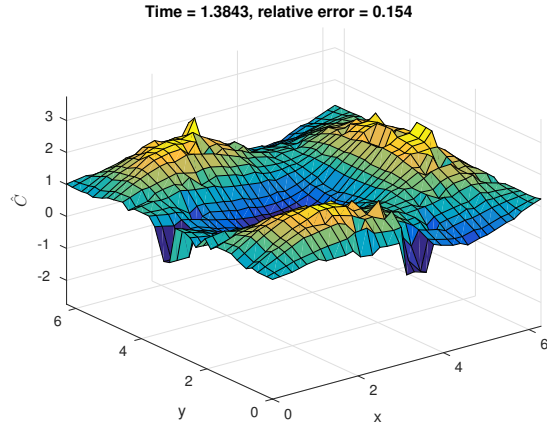




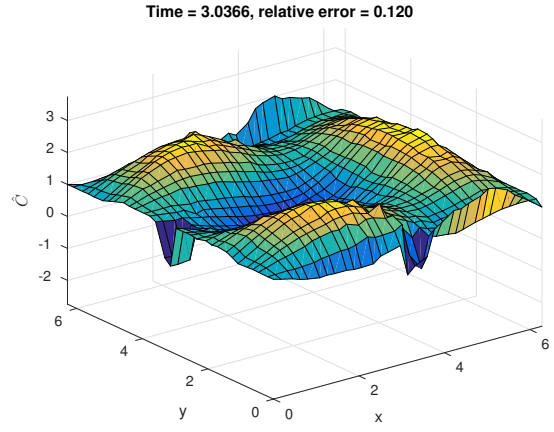
(a) Estimate at  $t = 0.1042$



(b) Estimate at  $t = 0.7343$

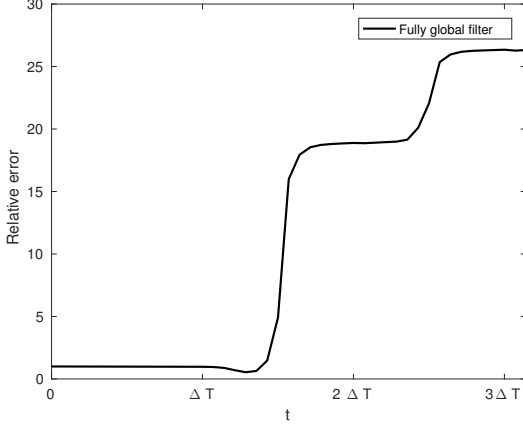


(c) Estimate at  $t = 1.3843$

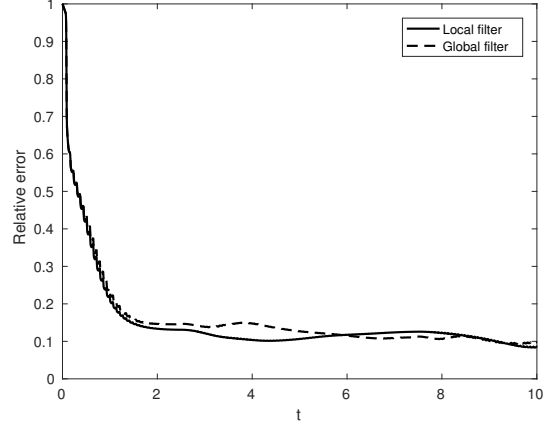


(d) Estimate at  $t = 3.0366$

Figure 3: Assimilation of a partial observations with precise boundary conditions and velocity field (Synthetic Test 2)



(a) Relative error for fully global filter



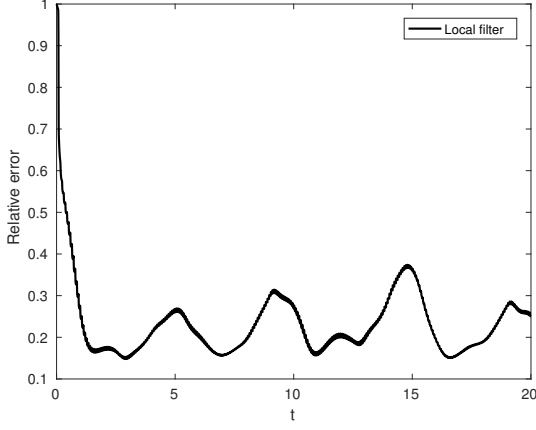
(b) Relative error for local and modified global filters

Figure 4: Relative error for partial observations with precise boundary conditions and velocity field (Synthetic Test 2)

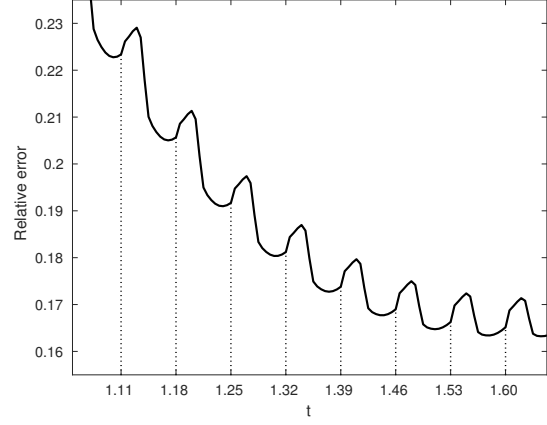
latter will not “see” the discontinuities induced by sparse observations, and consequently, neither will the global gain,  $P$ . In this case, the performance of the filter is similar to that of the distributed filter, as seen in fig. 4b, where, at  $t = 10$ , the relative error is  $\approx 0.09$  for the distributed filter and  $\approx 0.1$  for the global filter. This is not surprising, since the gain in either case is influenced by the same information, as explained in section 4.1.1. An important point to make is that the apparent advantage of the fully global filter (discussed in section 4.1.1) is gone when discontinuities due to observation sparsity are present. While having the system matrix absorb all but the boundary terms is generally preferable because of the richer information available to the filter, we saw that in the case of sparse observations, the discontinuities generated may cause the filter to fail. We also note that in the experiment with full observations, the fully global filter performed well, which supports our assertion that the presence of discontinuities due to observation sparsity was responsible for the failure of that filter.

#### 4.1.4 Synthetic Test 3: Sparse observations in space with imprecise knowledge of boundary conditions and velocity field

The next synthetic experiment we perform is with the same “chequered” observations but with imprecise boundary conditions and advection velocity field. To do this, we use (26) and (25) with a time-shift,  $t_s$ . In this way, the advection field and boundary conditions for the filter are out of phase with those used to generate the observations,  $\mathbf{Y}_s$ . We set  $b = b_\partial = 1$  and  $q = q_\partial = (N + 1)^2$ . In fig. 5a, we see the relative error of the distributed filter over time when we run the filter with a time-shift of  $t_s = -1.5$  for both the advection field and boundary conditions. Not only is the error generally higher than in the case of *Synthetic Test 2*, it is also seen to fluctuate over time. This appears to be due to the boundary conditions and advection field, which are periodic in time. This emphasises the impact of incorrect model parameters on the estimate; although high trust is placed in the observations, the incorrect model steers the estimate off track. The filter appears to perform better when the disparity between the assumed and real boundary conditions and advection field are small, which in this example occurs periodically. In fig. 5b, the error over relatively short time interval is shown, where the times at which data become available are indicated by vertical dashed lines. Here, we can see the change in error as the trust is varied over each time-step, and how this



(a) Relative error for distributed filter



(b) Relative error for distributed filter over short time

Figure 5: Relative error for partial observations with imprecise boundary conditions and velocity field (Synthetic Test 3)

is counteracted by the model which steers the estimate away from the truth. The absolute error at a single node for both the local and global filters is shown in fig. 6 for a short time interval. Also shown is the square root of the worst-case estimation error (20), i.e. the square root of the diagonal entry of the gain  $P^k$  for the node in question. We see that both the gains and the errors

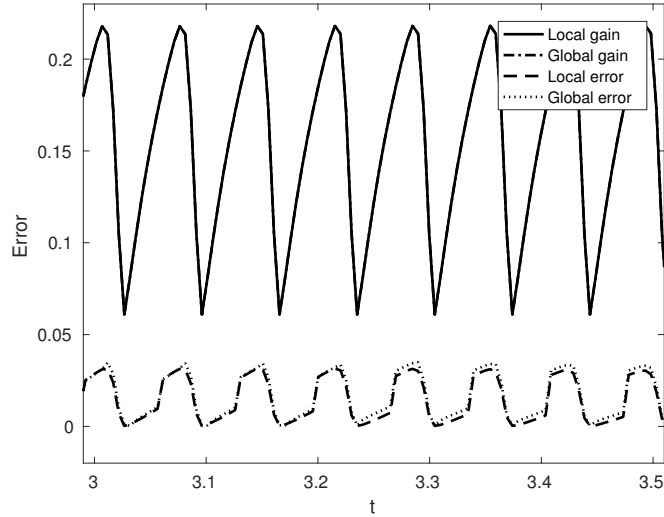


Figure 6: Square root of the worst-case estimation error and estimate error at single node for partial observations with imprecise boundary conditions and velocity field (Synthetic Test 3)

for local and global are close, as expected, and that the error is bounded by the square root of the gain entry as required.

#### 4.1.5 Computational complexity and scalability

Here we provide a very high level description of the computational cost measuring the latter in terms of the number of linear solves required to make an estimate for one time step. In the case of the global filter we need to perform one sparse linear solve with a matrix of dimension  $2(N+1)^2 * K$ , where  $N$  is the degree of the Lagrange polynomials, and  $K$  is the number of elements used for the DG method. The matrices  $A$  and  $A_b$  are however, sparse with the number of non-zero terms  $< 1\%$ , so a fast algorithm for sparse matrices such as GMRES [18] could be used for linear solves involving this matrix. However, the matrices  $U$  and  $V$  in (22) are dense, and the computation of  $P = VU^{-1}$  at each time-level requires  $K(N+1)^2$  linear solves with the matrix  $U$ , which is of dimension  $K(N+1)^2 \times K(N+1)^2$ . So, effectively, we need to invert  $U$  which costs at least  $O((N+1)^6 K^3)$  operations (for Gaussian elimination type linear solvers). Finally, to obtain the estimate using (23), a matrix of dimension  $K(N+1)^2 \times K(N+1)^2$  containing the dense matrix  $P$ , must be inverted. In contrast, to compute the distributed filter at each element, one needs to perform the same number of linear solves as the global filter but with matrices whose dimension is a factor of  $K$  times smaller: namely, one sparse linear solve with a matrix of dimension  $2(N+1)^2 \times 2(N+1)^2$  and so on. In particular, in this case inverting  $U$  costs  $O((N+1)^6)$  so, in total, we need  $O((N+1)^6 K)$  inversions. As a result, the total cost of computing the distributed filter scales linearly with  $K$  whereas for the global case the total computational cost is at least polynomial in  $K$ . Note that it is also possible to devise a hybrid or “semi-local” approach whereby neighbouring elements are grouped into regions on which a system matrix  $A^k$  is assembled from the elemental mass and stiffness matrices of the elements in the regions. In this case the computational cost of the distributed filter will be different.

To illustrate the scalability of the algorithm, we measure the CPU time taken to carry out the assimilation of a single set of observations for grids of different resolutions. This process requires the filtering to be performed  $n_s$  times in order to ramp up the trust in the observations (see section 3.4). In these experiments,  $n_s = 14$ . The results are shown in fig. 7. We see that the cost scales linearly

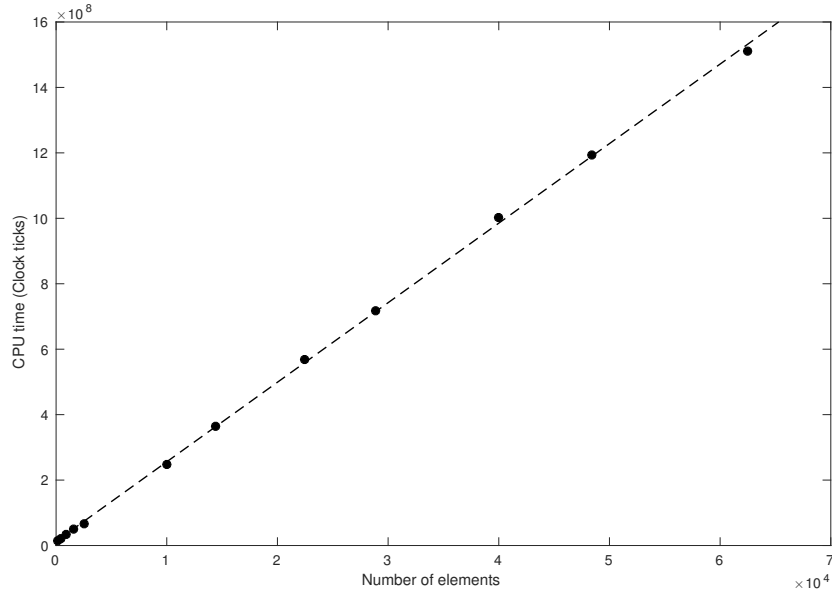


Figure 7: CPU time taken to assimilate one observation vs number of elements in DG grid

with the number of elements, as expected. The highest resolution grid depicted in the figure has  $250 \times 250$  elements with  $N = 3$  (i.e., state of dimension  $10^6$ ). For that grid, the experimental setup

was the same as that in ‘Synthetic Test 2’ described in section 4.1.3 (i.e.,  $10 \times 10$  grid of alternating observation regions and knowledge of advection field and boundary conditions). The filter was run until  $t = 1.5$  by which time the relative error was  $\approx 0.17$ . This demonstrates the efficacy and tractability of the algorithm at high resolution. We implemented algorithm 1 in C++, and parallelised the element loop (over  $k$  in algorithm 1) using OpenMP. The numerical experiments have been conducted on an IBM POWER8 machine with 196 cores and 0.5TB of RAM.

## 4.2 Real data scenario: satellite image assimilation

The distributed filtering algorithm is next tested on real data. For this experiment, the observations consist of satellite images depicting cloud optical depth, available at 15-minute intervals. We use a domain which spans 16 degrees of longitude and 12 degrees of latitude which, in the region in question, covers approximately  $1.68 \times 10^6$  square kilometres. The domain is discretised into a  $70 \times 70$  element grid with  $N = 3$ , which is close to the resolution of the images. The resulting system is of dimension 19600, which is considerably higher than that in the synthetic case where it was 400.

### 4.2.1 Satellite image data and advection field

Using a purely synthetic velocity field to advect the satellite images is not desirable as the resulting motion may not appear natural. Instead, we compute a sequence of fields which capture the motion of the sequence of images approximately by employing an optical flow estimation procedure [19]. We will not describe the basic optical flow estimation here but note that the procedure does not necessarily produce a divergence-free velocity field. In order to obtain a divergence-free field, we perform a projection and reconstruction of the velocity using the standard vorticity-stream formulation commonly used to solve the incompressible (divergence-free) Navier Stokes equation. This procedure is described briefly below.

The scalar field, vorticity,  $\xi = (\nabla \times \mathbf{u}) \cdot \mathbf{e}_z$ , is obtained numerically from the optical velocity field and is then projected into the space,  $\text{span}\{\phi_n(x)\phi_m(y)\}_{|n|,|m| \leq N_f/2}$  of complex exponentials, yielding  $N_f + 1$  projection coefficients,  $a_{nm}$ , where  $|n|, |m| \leq N_f/2$ . Defining the stream function,  $\Psi$  using the Poisson equation,  $-\Delta\Psi = \xi$ , we can express the velocity components as  $u = \Psi_y$  and  $v = -\Psi_x$ . Decomposing the Laplacian operator by taking complex exponentials as eigenfunctions, we can reconstruct the velocity field using the corresponding eigenvalues,  $\lambda_{nm}$ , as follows:

$$\begin{pmatrix} u \\ v \end{pmatrix} = \begin{pmatrix} \sum_{n,m} \frac{a_{nm}}{\lambda_{nm}} \phi_n^y \phi_m^y \\ \sum_{n,m} \frac{a_{nm}}{\lambda_{nm}} \phi_n^x \phi_m^x \end{pmatrix}, \quad (29)$$

where  $\phi_n^x$  and  $\phi_n^y$  are the derivatives of the complex exponential basis functions with respect to  $x$  and  $y$  respectively. This field is divergence-free.

Note that a periodic basis is used to generate the divergence-free field. As the image sequence we use depicts rotation within the domain with little movement on the boundary, this basis is suitable.

The velocity field which advects the images is obtained using an optical flow estimation procedure on a similar set of images to the ones being assimilated. The reason we do not use the observations to obtain the optical flow velocity field is that we do not wish the state trajectory to precisely pass through the images; rather, the velocity field only roughly captures flow and is thus a source of uncertainty. This way, the images are used to steer the state of the model which will veer off track due to the imprecise velocity field. The images are interpolated onto the DG-LGL grid using bi-linear interpolation. An example of the advection field is shown in fig. 8.

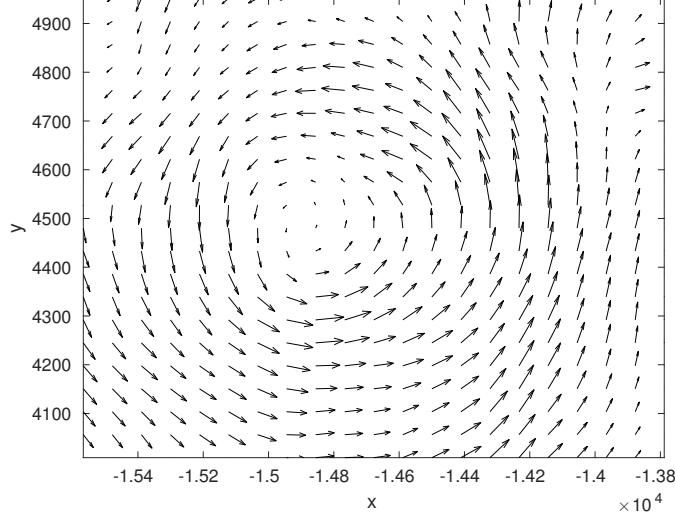


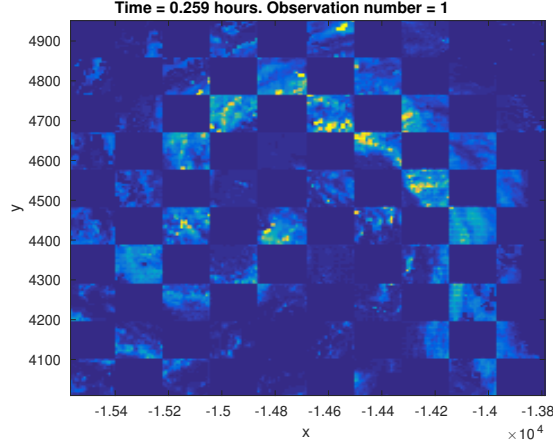
Figure 8: Sample velocity field for advection of satellite images

#### 4.2.2 Spatially and temporally sparse satellite observations

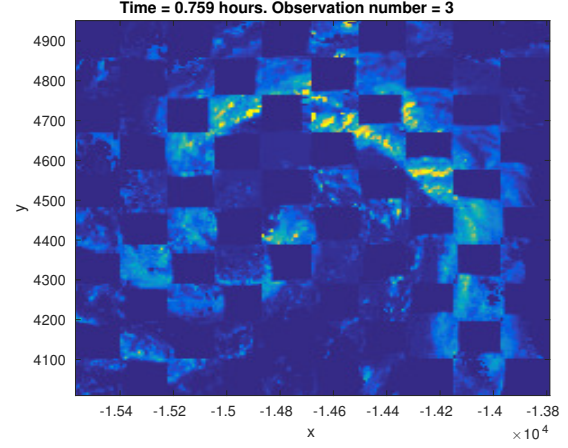
We perform an experiment to test the distributed filter with sparse observations by using the same “chequered” observation pattern that was used in section 4.1.3 and section 4.1.4 for the experiments on synthetic data in order to emulate partial image availability. However, instead of observing every other element, we observe the images on fixed  $7 \times 7$  blocks of elements, separated by blocks of the same size, giving a  $10 \times 10$  chequered observation pattern. The time-step,  $\Delta T$ , computed for the  $70 \times 70$  element grid with  $N = 3$ , is adjusted so that it fits the 15-minute interval, yielding  $\Delta T = 15/18$  minutes. Using this time-step, observations become available to the filter at intervals of 18 time-levels. This temporal sparsity can not be reduced for the current grid, as increasing  $\Delta T$  so that the observations are temporally less sparse would cause the system to violate the CFL condition. For the experiment, we initialise the state to zero, i.e.,  $\mathbf{C}_0 = 0$ , and impose zero Dirichlet boundary conditions at inflow nodes and free-exit Neumann conditions at outflow nodes.  $q$ ,  $q_0$  and  $q_\partial$  are initialised as in section 4.1.3 and  $b = b_0 = b_\partial = 1$ . The distributed filter is run for a simulated time of 3.5+ hours over which time it assimilates 14 observations. In fig. 9, the results are shown for 6 of those observations including the first and the last. The observation pattern is clear from fig. 9a where we see the alternating groups of  $7 \times 7$  elements with/without available observations. Over time, the error decreases, with the last observation yielding a relative error of  $\approx 0.16$ . Over time, the observation pattern does not change, so the portions of the domain without data rely on flux from neighbouring elements as we also saw in synthetic experiments in section 4.1.3 and section 4.1.4. We refer the reader to [1] for the further details on this.

## 5 Conclusions

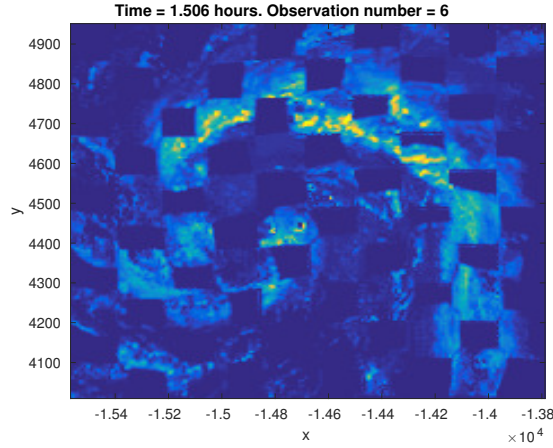
We conclude by summarising features of the proposed distributed filtering approach and outlining directions of the future research. The key advantage of the proposed filtering framework is its scalability: the computational cost of the distributed state estimator equals the cost of the filtering at each element multiplied by the total number of elements. Another important feature is the structure preserving discretisation at each element which preserves symmetry and positivity of the gain  $P^k$ , and all quadratic invariants of the estimation error dynamics. Finally, the filter is



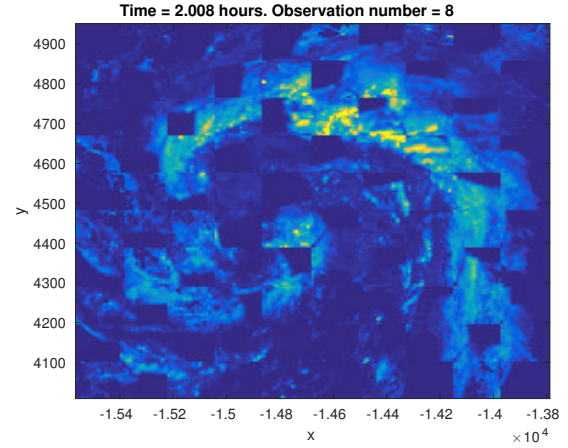
(a) Assimilation of 1st observation (Relative error  $\approx 0.56$ )



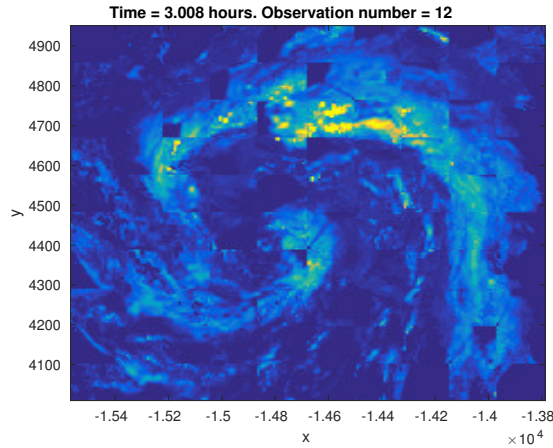
(b) Assimilation of 3rd observation (Relative error  $\approx 0.46$ )



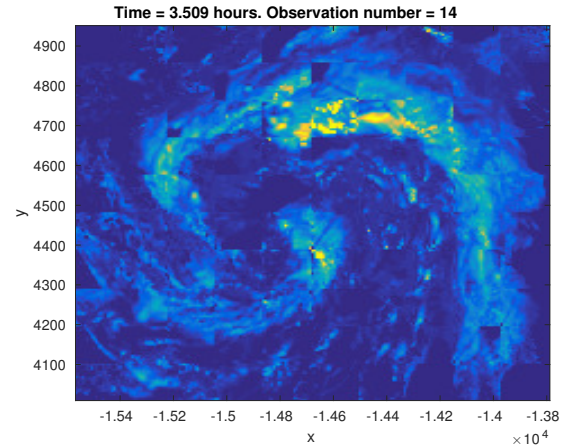
(c) Assimilation of 6th observation (Relative error  $\approx 0.35$ )



(d) Assimilation of 8th observation (Relative error  $\approx 0.28$ )



(e) Assimilation of 12th observation (Relative error  $\approx 0.20$ )



(f) Assimilation of 14th observation (Relative error  $\approx 0.16$ )

Figure 9: Assimilation of a partial satellite images with approximate divergence-free optical flow velocity field

designed for the hyperbolic equation directly, without introducing artificial viscosity. The latter is, to some extent, introduced by means of the Lax-Friedrichs flux which “smooths” out the jumps across inter-elemental boundaries. Experimental assessment of the distributed filters on synthetic and real data shows great potential of the algorithm.

A key direction for the future work is to study convergence of the proposed scheme, and introduce boundary interconnection mechanisms for the elemental Riccati equations to improve the uncertainty exchange mechanism.

## A Discontinuous Galerkin nodal mass and stiffness matrices

A convenient way to define the mass and stiffness matrices for 2D rectangular elements is to do so in terms of Legendre-Gauss-Lobatto (LGL) quadrature points and weights in the 1D interval  $I = [-1, 1]$  and also in terms of Lagrange polynomials defined on this interval. We denote the LGL quadrature points on  $I$  by  $\xi_i$  and  $w_i$  respectively, where  $i = 1 \dots N + 1$ . We can use  $\xi_i$  to define Lagrange polynomials on  $I$ ,

$$\ell_i(\xi) = \prod_{\substack{j=1 \\ j \neq i}}^{N+1} \frac{\xi - \xi_j}{\xi_i - \xi_j}, \quad (30)$$

which have the cardinal property,

$$\ell_i(\xi_j) = \delta_{ij}. \quad (31)$$

Due to this property, the mass matrix on  $I$  is given by  $M_I = \text{diag}(w_1 \dots w_{N+1})$ . We introduce the following mappings from elemental  $x$  and  $y$  intervals to the standard interval  $I$ ,

$$x(\xi) = x_l^k + \frac{1+\xi}{2} h_x^k \quad \text{and} \quad y(\xi) = y_l^k + \frac{1+\xi}{2} h_y^k, \quad x, y \in D^k \quad (32)$$

where  $\xi \in I$ , and  $x_l^k$  and  $x_r^k$  denote the left and right boundaries of the  $x$ -interval of element  $D^k$  whose  $x$ -length is  $h_x^k = x_r^k - x_l^k$ . The  $y$  quantities are defined analogously. We can now define the mass matrix on the intervals  $[x_l^k, x_r^k]$  and  $[y_l^k, y_r^k]$  as

$$M_x = \frac{h_x^k}{2} M_I \quad \text{and} \quad M_y = \frac{h_y^k}{2} M_I \quad (33)$$

respectively. Now, the mass matrix on a 2D element,  $D^k$ , can be defined as

$$M^k = M_x \otimes M_y. \quad (34)$$

In order to define the stiffness matrices, we first define matrices  $L$  and  $L_\xi$  which respectively contain grid functions of 1D Legendre polynomials and their derivatives on LGL points, i.e., the  $n$ -th column of  $L$  (resp.  $L_\xi$ ) contains a grid function representing the  $n$ -th Lagrange polynomial (resp. differentiated Lagrange polynomial) on the LGL points,  $\xi_i$ . Note that due to the cardinal property, (31),  $L$  is simply the identity matrix. We can now define the 2D elemental differentiation matrices,

$$D_{rx}^k = \frac{h_y^k}{2} (L_\xi \otimes L) \quad \text{and} \quad D_{ry}^k = \frac{h_x^k}{2} (L \otimes L_\xi), \quad (35)$$

which, when acted on a grid function on an element  $D^k$ , return another grid function approximating the derivative of that function with respect to  $x$  and  $y$  respectively. Defining the mass matrix on a standard element,  $I \times I$ , as  $M_{I \times I} = M_I \otimes M_I$ , the stiffness matrices are defined as,

$$S_x = M_{I \times I} D_{rx}^k \quad \text{and} \quad S_y = M_{I \times I} D_{ry}^k. \quad (36)$$



## B Proofs

*Proof of proposition 1.* Let  $\mathbf{C}_h^k$  solve (14). Then  $\mathbf{C}_h^k = \bar{\mathbf{C}}_h^k + \tilde{\mathbf{C}}_h^k$ , provided  $\bar{\mathbf{C}}_h^k$  solves  $\frac{d\bar{\mathbf{C}}_h^k}{dt} = A^k(t)\bar{\mathbf{C}}_h^k + \mathbf{B}^k$ ,  $\bar{\mathbf{C}}_h^k(0) = \mathbf{C}_0^k$ , and  $\frac{d\tilde{\mathbf{C}}_h^k}{dt} = A^k(t)\tilde{\mathbf{C}}_h^k + V^k\tilde{\mathbf{e}}^k(t)$ ,  $\tilde{\mathbf{C}}_h^k(0) = B_0^k\mathbf{e}_0^k$ . Define  $\tilde{\mathbf{Y}}^k := \mathbf{Y}^k - \bar{\mathbf{C}}_h^k$ , set  $p := (N+1)^2$ , and let us find  $\hat{u} \in L^2(t_0, t_f, R^p)$  such that,  $\forall u \in L^2(t_0, t_f, R^p)$ :

$$\max_{\tilde{\mathbf{e}}^k, \mathbf{e}_0^k, E\boldsymbol{\eta}^k(\boldsymbol{\eta}^k)^\top} \sigma(\hat{u}) \leq \max_{\tilde{\mathbf{e}}^k, \mathbf{e}_0^k, E\boldsymbol{\eta}^k(\boldsymbol{\eta}^k)^\top} \sigma(u), \quad \sigma(u) := E(\ell^\top \tilde{\mathbf{C}}_h^k(t+s) - \int_t^{t+s} u^\top \tilde{\mathbf{Y}}^k d\tau)^2,$$

provided that (15) and (6) hold true. Here  $\ell \in R^p$  is some vector. Introducing adjoint variable  $\frac{dz}{dt} = -(A^k)^\top z + (H^k)^\top u$ ,  $z(t+s) = \ell$ , and integrating by parts we find:

$$\sigma(u) = \left( z^\top(t)(B_0^k\mathbf{e}_0^k) + \int_t^{t+s} z^\top(V^k\tilde{\mathbf{e}}^k)d\tau \right)^2 + E \left( \int_t^{t+s} u^\top \boldsymbol{\eta}^k d\tau \right)^2$$

By using Cauchy-Schwartz inequality, (15) and (6) we find:

$$\max_{\tilde{\mathbf{e}}^k, \mathbf{e}_0^k, E\boldsymbol{\eta}^k(\boldsymbol{\eta}^k)^\top} \sigma(u) = (1+2s)(N+1)^2(z^\top(t)B_0^k(Q_0^k)^{-1}B_0^kz(t) + \int_t^{t+1} z^\top(V^k(\tilde{Q}^k)^{-1}(V^k)^\top)z + u^\top(R^k)ud\tau)$$

By using standard LQ control theory results [6] we find that the unique minimum point of this quadratic cost functional along the solutions of the adjoint equation for  $z$  satisfies the following feed-back representation:  $\hat{u} = (R^k)^{-1}H^kP^kz$ . By using the latter, and integration by parts it is not hard to find that:  $\int_t^{t+s} \hat{u}^\top \tilde{\mathbf{Y}}^k d\tau = \ell^\top \hat{\mathbf{C}}_h^k(t+s)$ , provided  $\hat{\mathbf{C}}_h^k$  solves

$$\frac{d\hat{\mathbf{C}}_h^k}{dt} = A^k\hat{\mathbf{C}}_h^k + P^k(H^k)^\top(R^k)^{-1}(\tilde{\mathbf{Y}}^k - H^k\hat{\mathbf{C}}_h^k), \quad \hat{\mathbf{C}}_h^k(0) = 0.$$

Integrating by parts we find:

$$\max_{\tilde{\mathbf{e}}^k, \mathbf{e}_0^k, E\boldsymbol{\eta}^k(\boldsymbol{\eta}^k)^\top} \sigma(\hat{u}) = E(\ell^\top \tilde{\mathbf{C}}_h^k(t+s) - \ell^\top \hat{\mathbf{C}}_h^k(t+s))^2 = (1+2s)(N+1)^2\ell^\top P^k(t+s)\ell \quad (37)$$

Now, by recalling that  $\mathbf{C}_h^k = \bar{\mathbf{C}}_h^k + \tilde{\mathbf{C}}_h^k$ , and by noting that, in fact:  $\hat{\mathbf{C}}_h^k = \bar{\mathbf{C}}_h^k + \tilde{\mathbf{C}}_h^k$  we obtain (20) from (37) by setting  $\ell = (0 \dots 010 \dots 0)^\top$ , where 1 is at position  $j$ . This completes the proof.  $\square$

## References

- [1] A. Akhriev, T. Tchraikian, S. Lu, and S. Zhuk. Dynamic cloud motion forecasting from satellite images. In *Proc. of IEEE Conference on Decision and Control*, 2017.
- [2] C. Bardos. Problèmes aux limites pour les équations aux dérivées partielles du premier ordre à coefficients réels: théorèmes d'approximation; application à l'équation de transport. *Ann. scient. Ec. Norm. Sup.*, 3(4):185–233, 1970. (in french).
- [3] B. Cockburn and C.-W. Shu. TVB Runge–Kutta local projection Discontinuous Galerkin finite element method for conservation laws. II. general framework. *Mathematics of computation*, 52(186):411–435, 1989.

- [4] B. Cockburn and C.-W. Shu. Runge–Kutta Discontinuous Galerkin methods for convection-dominated problems. *Journal of Scientific Computing*, 16(3):173–261, 2001.
- [5] G. Evensen. Sampling strategies and square root analysis schemes for the enf. *Ocean Dynamics*, (54):539–560, 2004.
- [6] J. Frank and S. Zhuk. Symplectic möbius integrators for lq optimal control problems. In *Proc. of IEEE Conference on Decision and Control*, 2014.
- [7] I. Gihman and A. Skorokhod. *Introduction to the Theory of Random Processes*. Dover Books on Mathematics. Dover, 1997.
- [8] J. Hesthaven and T. Warburton. *Nodal Discontinuous Galerkin Methods: Algorithms, Analysis, and Applications*. Texts in Applied Mathematics. Springer, 2008.
- [9] A. J. Krener. Kalman-Bucy and minimax filtering. *IEEE Trans. on Autom. Control*, 25(2):291–292, Apr 1980.
- [10] A. Kurzhanski and I. Vályi. *Ellipsoidal Calculus for Estimation and Control*. Birkhäuser Boston, 1997.
- [11] K. Law, A. Stuart, and K. Zygalakis. *Data Assimilation: a Mathematical Introduction*. Springer, 2015.
- [12] J. Malm, P. Schlatter, P. F. Fischer, and D. S. Henningson. Stabilization of the spectral element method in convection dominated flows by recovery of skew-symmetry. *Journal of Scientific Computing*, 57(2):254–277, 2013.
- [13] L. Pontryagin, V. Boltyanskii, R. Gamkrelidze, and E. Mishchenko. *The Mathematical Theory of Optimal Processes*. English translation: Interscience, 1962.
- [14] J. Qiu and C.-W. Shu. Runge–Kutta Discontinuous Galerkin method using WENO limiters. *SIAM Journal on Scientific Computing*, 26(3):907–929, 2005.
- [15] A. Quarteroni and A. Valli. *Numerical Approximation of Partial Differential Equations*. Series in Computational Mathematics. Springer, 2008.
- [16] P. Raviart. An analysis of particle methods. In F. Brezzi, editor, *Numerical Methods in Fluid Dynamics*, volume 1127 of *Lecture Notes in Mathematics*, pages 243–324. Springer.
- [17] S. Reich and C. Cotter. *Probabilistic Forecasting and Bayesian Data Assimilation*. Cambridge Univ. Press, 2015.
- [18] Y. Saad and M. H. Schultz. GMRES: A generalized minimal residual algorithm for solving nonsymmetric linear systems. *SIAM Journal on scientific and statistical computing*, 7(3):856–869, 1986.
- [19] D. Sun, S. Roth, and M. Black. A quantitative analysis of current practices in optical flow estimation and the principles behind them. *Int. J. Comput. Vis.*, (106):115137, 2014.
- [20] S. Zhuk. Estimation of the states of a dynamical system described by linear equations with unknown parameters. *Ukrainian Math. J.*, 61(2):214–235, 2009.
- [21] S. Zhuk, J. Frank, I. Herlin, and R. Shorten. Data assimilation for linear parabolic equations: minimax projection method. *SIAM J. Sci. Comp.*, 37(3):A1174–A1196, 2015.

- [22] S. Zhuk, A. Polyakov, and O. Nakonechniy. Note on minimax sliding mode control design for linear systems. *IEEE Transactions on Automatic Control*, 2016.